metals

MDPI

Article

Effect of Normalising Process on the Corrosion Behaviour of U75V Rail Flash Butt Welded Joints in a Marine Environment

Xi Zhang [1], Tingting Liao [2], Qibing Lv [1,*] and Guoqing Gou [1,*]

[1] School of Materials Science and Engineering, Southwest Jiaotong University, Chengdu 610031, China
[2] School of Materials and Environmental Engineering, Chengdu Technological University, Chengdu 611730, China
* Correspondence: xnjdlvqibing@163.com (Q.L.); gouguoqing1001@163.com (G.G.)

Abstract: U75V rail steel is widely used in railways in China, including train tunnels in mountain and subsea projects, where it suffers from selective corrosion near welded joints. To ensure adequate railway service life, this study examines the effect of the normalisation process on the electrochemical behaviour of U75V rail-welded joints (URWJs) manufactured by flash butt welding (FBW) using potentiodynamic polarisation and electrochemical impedance spectroscopy (EIS). Corrosion morphology and elemental distribution analyses were performed to investigate the corrosion behaviour. The results show that the grains within the joints became finer and more homogeneous after normalisation, with a lower corrosion rate and higher corrosion resistance. It is demonstrated that fewer corrosion products were formed on the surface of the normalised joints after electrochemical test, and the corrosion resistance of the URWJs improved, owing to the formation of denser passivation films caused by normalisation. These mechanisms of corrosion response help explain corrosion failure in railway lines, as well as also help optimise the welding process and normalising processes to obtain a corrosion-resistant microstructure and ensure the quality of welded joints.

Keywords: flash butt welding; U75V rail; normalising; corrosion behaviour

Citation: Zhang, X.; Liao, T.; Lv, Q.; Gou, G. Effect of Normalising Process on the Corrosion Behaviour of U75V Rail Flash Butt Welded Joints in a Marine Environment. *Metals* **2022**, *12*, 2146. https://doi.org/10.3390/met12122146

Academic Editor: Sergey Konovalov

Received: 17 November 2022
Accepted: 10 December 2022
Published: 14 December 2022

1. Introduction

As the Chinese high-speed railway network grows more extensive, flash butt welding (FBW) has become one of the most widely used welding techniques owing to its good appearance, high strength, and stability [1–3]. U75V welded joints (URWJs) produced by FBW are widely used in railway passenger lines and passenger cargo mixed lines, due to their stability, high strength, and ease of processing [4–6]. However, the microstructures of the welded joints undergo dramatic changes during the welding process, and defects inside the welded beam render it the weakest section of the rail. This issue directly affects the service life of the railroads [7–10]. During service, the URWJs of a rail track is subjected to complex and diverse environmental conditions, such as changes in humidity and temperature and exposure to corrosive media. [11–13]. Pits formed at the bottom of the welded joint lead to stress corrosion and fatigue fracture of the rail track (as shown in Figure 1 [14]). These failures can easily cause catastrophic accidents, especially in coastal regions and undersea tunnels, due to the harsher service environments in these locations, compared to inland areas [15–17].

The corrosion response is the main initial reaction of a welding joint in a complex environment. It is a synergistic and self-reinforcing process that depends on the characteristics of the welding joints [18–20]. Many researchers have investigated the relationship between the corrosion behaviour of the microstructure and the mechanical properties of welding joint materials. Sinhmar et al. studied the corrosion behaviour of friction stir-welded and tungsten inert gas-welded AA2014 aluminium alloys [21]. Xu et al. experimentally analysed the correlation between the microstructure and corrosion behaviour of copper/316 L stainless-steel dissimilar metal welded joints on an electrolytic copper cathode plate [22]. Liu et al. examined the corrosion behaviour of Mg–steel laser–TIG hybrid lap joints [23].

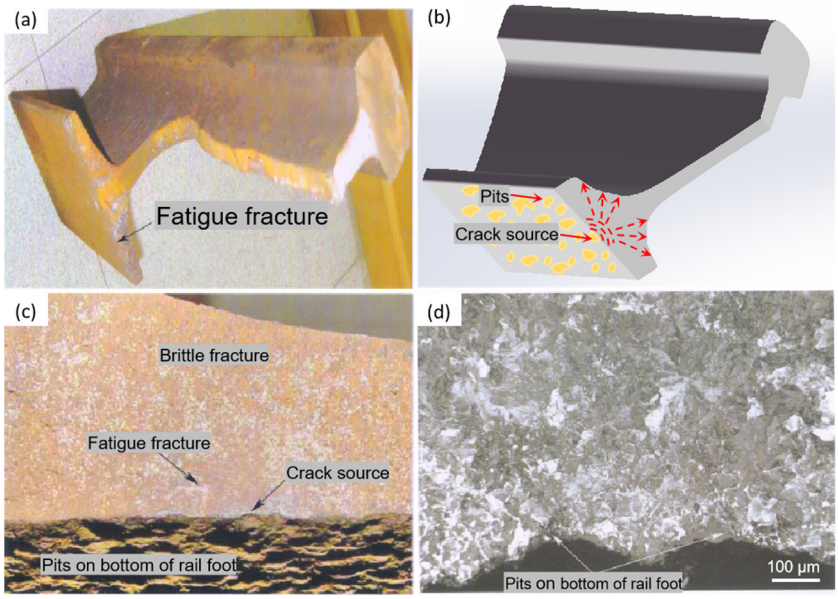

Figure 1. Fatigue fracture of the joint: (**a**) Fatigue fracture; (**b**) the schematic diagram of pits; (**c**) pits on bottom of rail foot; (**d**) metallographic structure around pits.

Regarding the URWJs of FBW, most studies have concentrated on the influence of the welding procedure on the joint microstructure, mechanical properties, and the number of defects. Ziemian et al. tested the effects of flashing and upset sequences on the microstructure, hardness, and tensile properties of welded structural steel joints [24]. Zhao et al. investigated the fatigue fracture mechanism of FBW joints of U75V rail steel. They observed that the corrosion fatigue life was significantly reduced in samples that had been corroded beforehand [13]. Porcaro et al. analysed the microstructure and mechanical properties of an FBW pearlitic rail using a dilatometry-based methodology [2]. Bauri et al. investigated the effects of welding parameters on the control of the microstructure and mechanical properties of rails welded using FBW [25]. However, no study has specifically examined the corrosion behaviour of rail joints using FBW, and there are few studies on U75V rail steel joints produced by FBW.

Additionally, the railway standards of different countries have different requirements for the post-welding heat treatment (PWHT). According to the Chinese railway standard [26], the URWJs must be normalised before rail laying. In contrast, the European rail welding standard does not require normalisation.

Therefore, this study mainly investigated the corrosion mechanism of FBW joints of U75V rail steel, focusing on the effect of the normalising process on electrochemical behaviour, to determine corrosion reaction mechanisms by comprehensively considering the welding process, metallographic characteristics and hardness of the joints. This research will help to improve the quality of continuous welded rails, particularly in coastal areas and subsea tunnels.

2. Materials and Method

2.1. Preparation of U75V Welded Joints

In this study, U75V rail steel used as the base metal (BM) was manufactured by PanZhiHua Iron and Steel, Sichuan, China, and corresponds to a high carbon and eutectoid composition. Its main chemical compositions and mechanical properties are listed in Tables 1 and 2, respectively. A model UN5-150ZB1 flash welding device (Chengdu Aige Technology Co., Ltd., Chengdu, China) was used to perform the FBW of the U75V rail steel. The pulsating FBW process consisted of five stages, namely preheating flash, pulse flash, steady flash, acceleration flash, and upsetting. The URWJs were normalised by flame heating according to the Chinese railway welding standard [26]. The schematic of the joint

is shown in Figure 2. The welded joints before and after the normalisation process are abbreviated as URWJB and URWJA, respectively. The URWJs by FBW can be divided into three areas (Figure 2b,c), namely BM, heat-affected zone (HAZ), and weld metal (WM). The WM of FBW is also known as the fusion line (approximately 1 mm wide) and can be seen in the middle of the joints. The width of the HAZ of the URWJB is approximately 28–41 mm, and it expands to 76–94 mm after normalisation.

Table 1. Chemical composition of U75V rail steel (wt. %).

C	Si	Mn	S	P	V	Fe
0.71~0.8	0.50~0.80	0.75~1.05	<0.025	<0.02	0.04~0.12	Balance

Table 2. Mechanical properties of U75V rail steel.

Yield Strength Rp0.2 (MPa)	Tensile Strength Rm (MPa)	Elongation A (%)	Hardness of Rail Head (HB)
>510	>980	>10	280–320

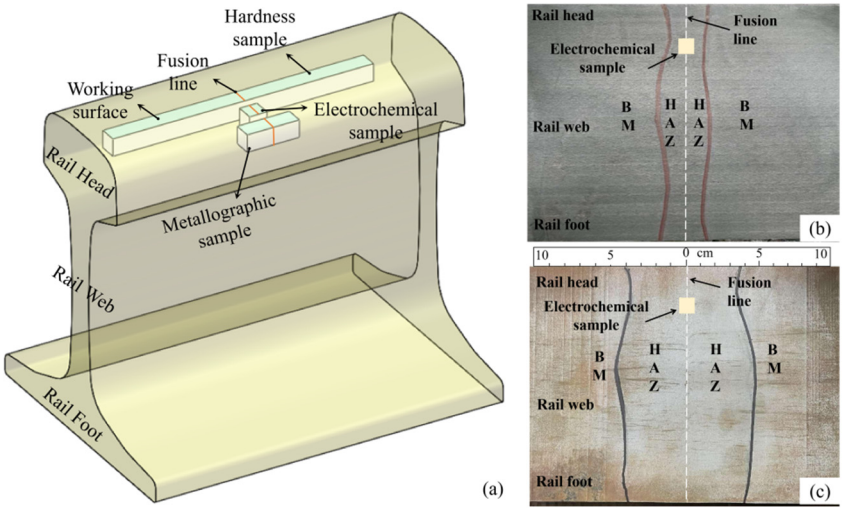

Figure 2. Schematic of the joint: (**a**) Schematic of sample cutting; cross-section morphology of the (**b**) URWJB and (**c**) URWJA.

2.2. Electrochemical Tests

To determine the electrochemical properties of the URWJs, samples with dimensions of 10 mm × 10 mm × 10 mm were cut from the welded joint and the BM, as shown in Figure 2a. Apart from the working surface, the remaining of the specimens were packed with 704 silica gel. After complete curing, the working surface of the sample was mechanically polished to obtain a scratch-free surface, and this was followed by ultrasonic cleaning with an alcohol solution for 15 min. Potentiodynamic polarisation testing and electrochemical impedance spectroscopy (EIS) analyses were performed using a CS310 electrochemical workstation. The sample was connected to a working electrode (1 cm^2), in which the platinum and saturated calomel electrodes served as the auxiliary and reference electrodes, respectively.

Before the polarisation and EIS tests, the samples were immersed in a simulated sea-water solution for 30 min to equilibrate. Subsequently, the open-circuit potential was stabilised by providing an initial 30 min delay. The potentiodynamic polarisation (PDP) curve was recorded at a scanning rate of 0.5 mV/s and a potential range from −500 mV to +500 mV relative to the OCP. The self-corrosion potentials and self-corrosion current densities were obtained from the PDP curves using the Tafel linear extrapolation method. EIS measurements were performed at frequencies between 100 kHz and 0.01 Hz with an

AC amplitude of 10 mV, and the EIS results were fitted using the Z-sim/Z-ft software based on the equivalent circuit models. Each experiment was repeated at least three times under the same condition to confirm reproducibility. All the electrochemical measurements were conducted in the simulated sea solution at room temperature (25 °C). The compositions of the simulated sea solutions are listed in Table 3.

Table 3. Chemical composition of the artificial seawater.

Salt	Concentration
NaCl	105.00
$MgCl_2$	12.7
$MgSO_4 \cdot 7H_2O$	7.7
$CaSO_4 \cdot 2H_2O$	12.15
$CaCO_3$	0.5

2.3. Metallographic Tests

The metallographic morphologies of the microstructures of the materials were observed using optical microscopy (AxioLab.A1, ZEISS, Oberkochen, Germany) and scanning electron microscopy (SEM, JSM 7800F Prime, JEOL, Tokyo, Japan). The applied voltage and working depth for the SEM test were 2.7 kV and 8 mm, respectively. The microhardness of the materials was evaluated using a Vickers hardness test (HXD-100TM/LCD, Optical-SH, Shanghai, China), and the position was tested every 2 mm with a load of 9.8 N.

To compare the localised corrosion behaviours of the welded joint, after the electrochemical test, the specimens were ultrasonically cleaned with ethanol to monitor the corrosion morphologies using SEM (Gemini, ZEISS, Germany), and the elemental distributions were analysed using an energy-dispersive spectrum (EDS) detector.

3. Results and Discussion

3.1. The Microstructure Analysis

Figure 3 shows the metallographic microstructure of the BM. As shown in Figure 3a, abundant lamellar pearlite structures and a small amount of ferrite are observed in the BM's structure. The interlamellar spacing was measured under higher amplification, and it was found to be approximately 0.3 μm (Figure 3b). According to the Chinese industrial standards [26,27], the metallographic structure of U75V rail steel, welded joints, and HAZ should be pearlite. A small amount of ferrite was permitted, whereas martensite, bainite, and cementite located at the grain boundaries were strictly controlled. In the FBW process, the joint temperature can reach 1300 °C and the microstructure of the WM produces austenite with coarse grains, leading to hard and brittle joints.

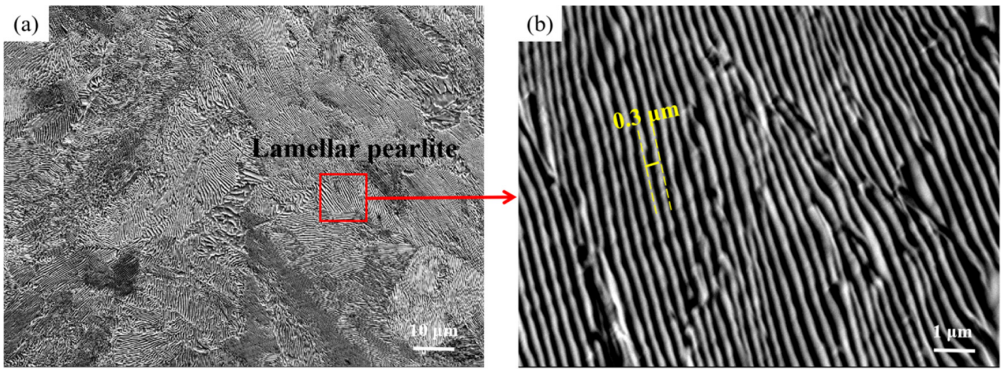

Figure 3. (**a**) Metallographic structure of BM, (**b**) magnified interlamellar spacing of pearlite.

Figure 4 shows the metallographic microstructures of the FBW joints before and after normalisation. A typical fusion line structure of the welding seam can be observed in Figure 4a,d, and the main structure consists of pearlite and a small amount of ferrite. The

grain size of the URWJB (approximately 90 μm) is larger and less uniform than that of the URWJA. The recrystallisation during normalisation process caused the coarse grains to become finer (16 μm grain diameter) and more homogeneous (Figure 4a–e). The resultant fine-grained structure improved joint strength and toughness. Figure 4c,f shows the interlamellar spacing of pearlite in the URWJB and URWJA samples, respectively. The interlamellar spacing of WM (around 0.2 μm, both in URWJB and URWJA) is much smaller than that of BM (0.3 μm), which leads to a higher hardness value for WM compared to that of BM.

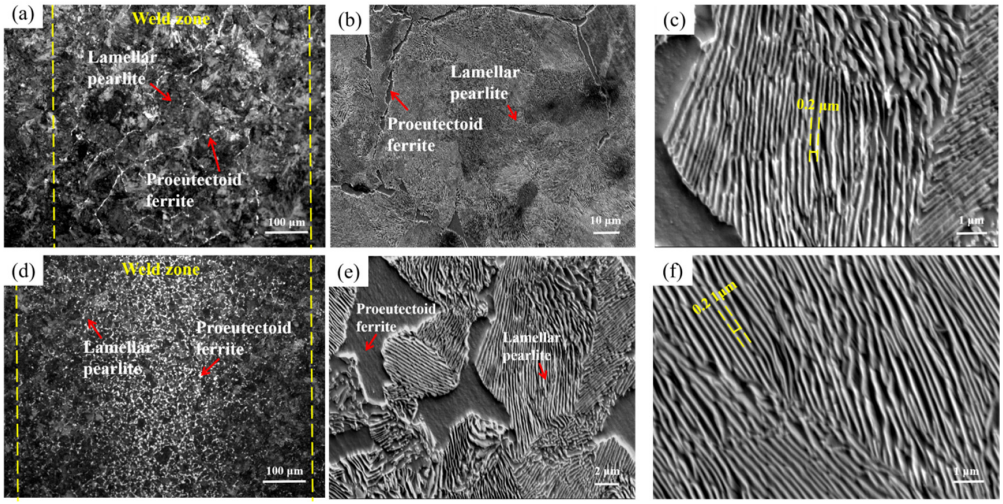

Figure 4. Metallographic structure of (**a**) URWJB and (**d**) URWJA. Microstructure near grain boundaries of (**b**) URWJB and (**e**) URWJA, interlamellar spacing of pearlite of (**c**) URWJB and (**f**) URWJA.

3.2. The Hardness Analysis

As shown in Figure 5a,b, the Vickers hardness of the BM has a uniform distribution, and all the welded joints present the same "W" hardness distribution (higher value and larger fluctuations than those of the BM). The average Vickers hardness of BM (Hp) was 293 HV and those of URWJB and URWJA were 322 and 306 HV, respectively. Furthermore, a softened zone with a width of 2 mm was observed on both sides of the welding zone in URWJB (Figure 5a). In contrast, URWJA exhibited a lower average hardness and a wider softened zone (10 mm on either side, Figure 5b). In addition, the maximum hardness value of URWJB was higher than that of URWJA. Previous studies have demonstrated that coarse grains of welded joints lead to higher hardness and lower toughness [28,29]. The significant decrease in hardness is attributed to partial cementite spheroidisation in the HAZ [2]. These data suggest that a smaller and more homogeneous hardness distribution can be found in the joints after the normalisation process, which is consistent with the microstructure results.

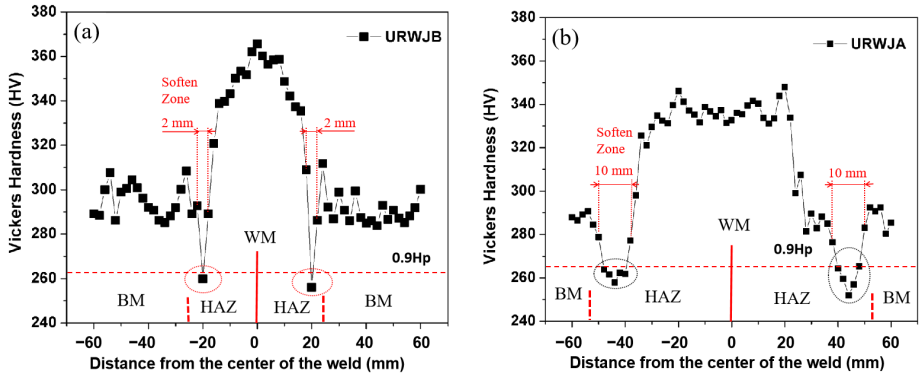

Figure 5. The Vickers hardness of FBW joints: (**a**) URWJB, (**b**) URWJA.

3.3. Polarisation Curve

As shown in Figure 6 and Table 4, the self-corrosion currents of the BM, URWJB, and URWJA are 1.12×10^{-4}, 4.84×10^{-4}, and 1.83×10^{-4} A/cm^2, with the corresponding self-corrosion potentials of −0.803, −0.828, and −0.850 mV, respectively. Compared with BM, URWJs exhibited higher self-corrosion currents and more negative self-corrosion potentials, indicating a higher corrosion rate and worse corrosion resistance. The polarisation curves of the URWJs gave similar results for both the URWJB and URWJA. Compared with the URWJB samples, the URWJA joints exhibited a smaller self-corrosion current, indicating a lower corrosion rate and a better corrosion resistance. Moreover, passivation was observed in the polarisation curves of both the welded joints. Although URWJA shows a slightly more negative corrosion potential (−0.850 mV), passivation occurs more easily in URWJA, and hence, the passivation coating protects the material from further corrosion response.

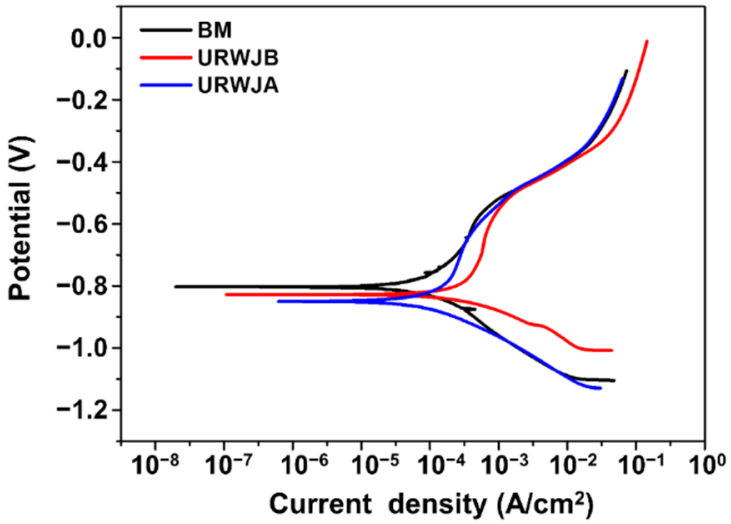

Figure 6. Cyclic potentiodynamic polarisation curves of BM and URWJs.

Table 4. Results obtained from the potentiodynamic polarisation test.

Samples	Self-Corrosion Potential (mV)	Self-Corrosion Current (A/cm^2)	Corrosion Rate (mm/A)
BM	−0.803	1.12×10^{-4}	1.309
URWJB	−0.828	4.84×10^{-4}	5.647
URWJA	−0.850	1.83×10^{-4}	2.162

3.4. EIS Analysis

To understand the corrosion mechanisms of URWJs in a marine environment, we further investigated the corrosion characteristics of the materials by combining them with EIS tests. Figure 7 shows the EIS plots of the BM and URWJs. The electrical equivalent circuit (EEC) used to fit the experimental data is shown in Figure 7. All Nyquist plots were characterised by an incomplete elliptical capacitive loop, a feature which was potential-dependent. The diameter of the semicircle in the Nyquist plot was based on the corrosion-resistance value. It was observed that the diameter of the URWJA was larger than that of the URWJB. These data suggest that the diameter of the capacitive arc in the Nyquist plot increased after the normalisation process, indicating an increase in corrosion resistance in the marine environment after normalisation.

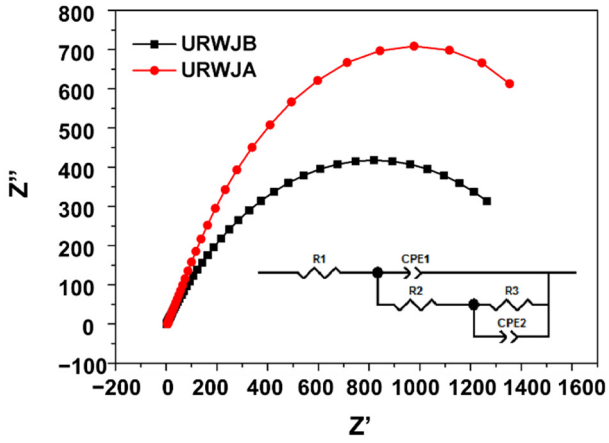

Figure 7. Nyquist plots of BM and URWJs.

In the Bode plots shown in Figure 8a, the impedance modulus value remains almost constant at high frequencies, and the phase angle is close to zero, indicating resistive-like behaviour [30]. At medium and low frequencies, a slanted impedance modulus value and a maximum phase angle below −90° are achieved, suggesting capacitive-like behaviour and a pseudocapacitive nature of the passive films [31]. In terms of the maximum phase angle, that of the BM (approximately 88°) is higher than those of the joints. The maximum phase angle of the URWJA (approximately 58°) was slightly larger than that of the URWJB (approximately 51°), indicating an improvement in the maximum phase angle of the joints after the normalising process.

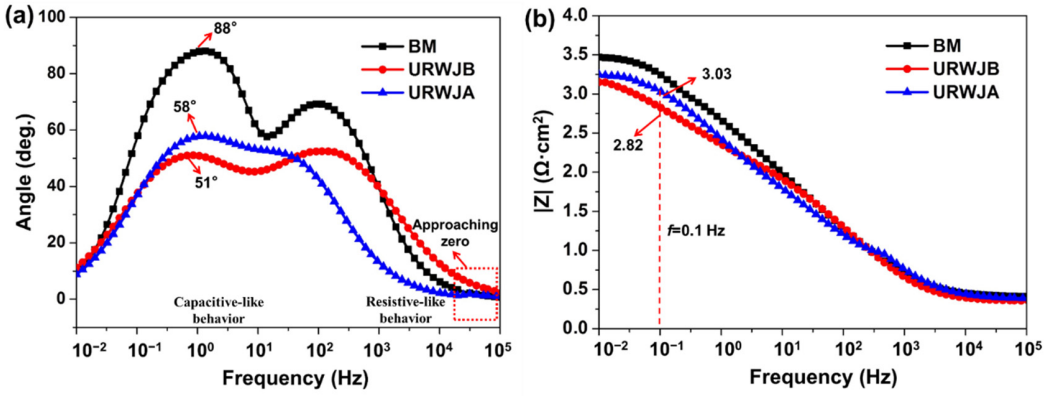

Figure 8. Bode plots of BM and URWJs: the relationship between (**a**) phase angle and log *f*, (**b**) log |Z| and log *f*.

Figure 8b shows the linear relationship between log |Z| and log *f* in the frequency range 10^{-2}–10^{5} Hz. The value of |Z| at a fixed frequency (0.1 Hz) in the Bode plots typically corresponds to the polarisation resistance, which reflects the corrosion resistance of the joints in a simulated sea solution [32]. As observed in Figure 8b, the values of |Z| at 0.1 Hz for the URWJA samples (3.03 Ω·cm^2) were higher than that of the unnormalised joints (2.82 Ω·cm^2), indicating that the URWJA samples are more corrosion-resistant than the URWJB samples under marine conditions. This difference in corrosion resistance was attributed to the different compositions and structures of the passive films formed on the surfaces of the samples, which was further confirmed by the SEM and EDS results.

As shown in Table 5, the EEC model is composed of a solution resistance (R1), oxide layer resistance (R2), charge transfer resistance (R3), and constant phase element (CPE). The CPE parameter Q has been widely used in fitting impedance data owing to different corrosion phenomena [33,34]. Y_0 is the admittance, in which the circuit becomes a capacitor, resistor, or inductor at n = 1, 0, or −1, respectively, where n is the deviation of

the capacitance of the circuit from the ideal capacitor. An *n* value of less than 1 indicates a frequency-dependent capacitor which shows the characteristic behaviour of an oxide film. Additionally, an X^2 (chi-squared) test was used to verify the reliability of the EEC [21,22].

Table 5. Equivalent circuit element values of EIS test corresponding to URWJs by FBW.

Sample	R1 (Ω)	Y_0-Q_1 (Ω^{-1} cm^{-2} S^n)	n-Q_1	R2 (Ω cm^2)	Y_0-Q_2 (Ω^{-1} cm^{-2} S^n)	n-Q_2	R3 (Ω cm^2)	X^2 Chi-Squared	R1 + R2 + R3 (Ω cm^2)
BM	3.421	4.2662×10^{-6}	0.8408	4682	3.042×10^{-5}	0.4114	16,118	5.753×10^{-4}	20,308
URWJB	5.373	2.873×10^{-4}	0.7644	34.51	1.717×10^{-4}	0.7219	1712	2.563×10^{-4}	1751
URWJA	4.79	6.73×10^{-4}	0.7339	202.1	2.435×10^{-4}	0.8589	1774	8.984×10^{-4}	1980

Table 5 shows the EEC fitting parameters obtained for the URWJB and URWJA microzones under the OCP conditions. It can be seen that the total resistance of the URWJ samples after normalisation (1980 Ω^{-1} cm^2) was larger than that without normalisation (1751 Ω^{-1} cm^2). To be specific, a larger oxide layer resistance (R2) can be found in the URWJA (202.1 Ω^{-1} cm^2) compared to the URWJB (34.5 Ω^{-1} cm^2). The URWJ samples before normalisation showed a lower R3 value (1712 Ω^{-1} cm^2) than that after normalisation (1774 Ω^{-1} cm^2). This observation suggests that the passive film formed on the URWJ samples had more activated sites before normalisation, further reducing their corrosion resistance. This also indicates that the electrochemical reaction rate occurring at the passive film/electrolyte interface or the dissolution rate of the passive film was higher for the URWJB samples than for the URWJA samples under marine conditions.

3.5. Morphology Analysis

Figure 9 shows the corroded surface morphology of the U75V rail samples in a marine environment after electrochemical tests at room temperature. Typical mild corrosion was observed on the surface of the BM (Figure 9a,d) compared with those of the welded joints.

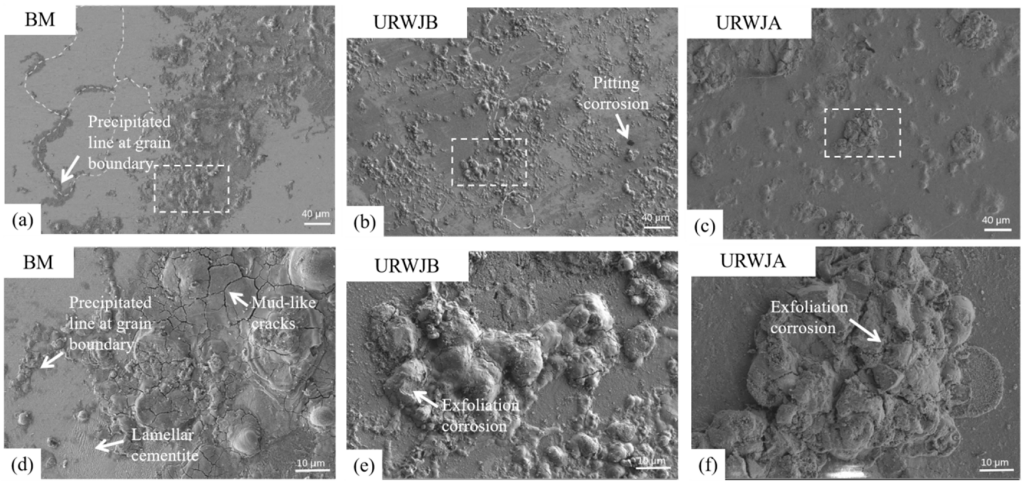

Figure 9. Morphology of samples after electrochemical test: BM, URWJB, URWJB.

Without normalisation, all the microzone surfaces of the URWJs were severely corroded after cyclic potentiodynamic polarisation, showing major non-uniform surface exfoliation and a large number of dispersive corrosion products (Figure 9b,e). After normalisation, the corrosion products were more densely distributed on the sample surface compared to the URWJB samples (Figure 9c,f). Thus, it is reasonable to conclude that the URWJB samples experienced more severe corrosion than the URWJA samples. This phenomenon can be attributed to the formation of compact and continuous corrosion products on the surface of the URWJA as the polarisation progressed, consistent with the results of the polarisation curve and EIS analysis.

3.6. Component Analysis

Figure 10a,d shows the locations of the SEM–EDS analyses of the U75V rail samples and the corresponding elemental compositions are listed in Table 6. Figure 10c–f shows the elemental distribution across the corroded surfaces. The EDS results show that the proportion of elemental chlorine, oxygen, and sulphur has significantly increased in the corroded areas compared to the other sites of the welded joints; in particular, the oxygen content increased more noticeably in comparison with the two other elements. This suggests that oxide is the main element of the corrosion product on the microzone surface. The results also show that Fe and Mn decreased in the corrosion product compared to the product-free microzone, suggesting that metallic elements readily dissolve in the marine solution. Fundamental to rail steel corrosion is the dissolution of iron [35], and it is believed that the initial stage of steel corrosion is the adsorption of reactive ions onto the steel surface.

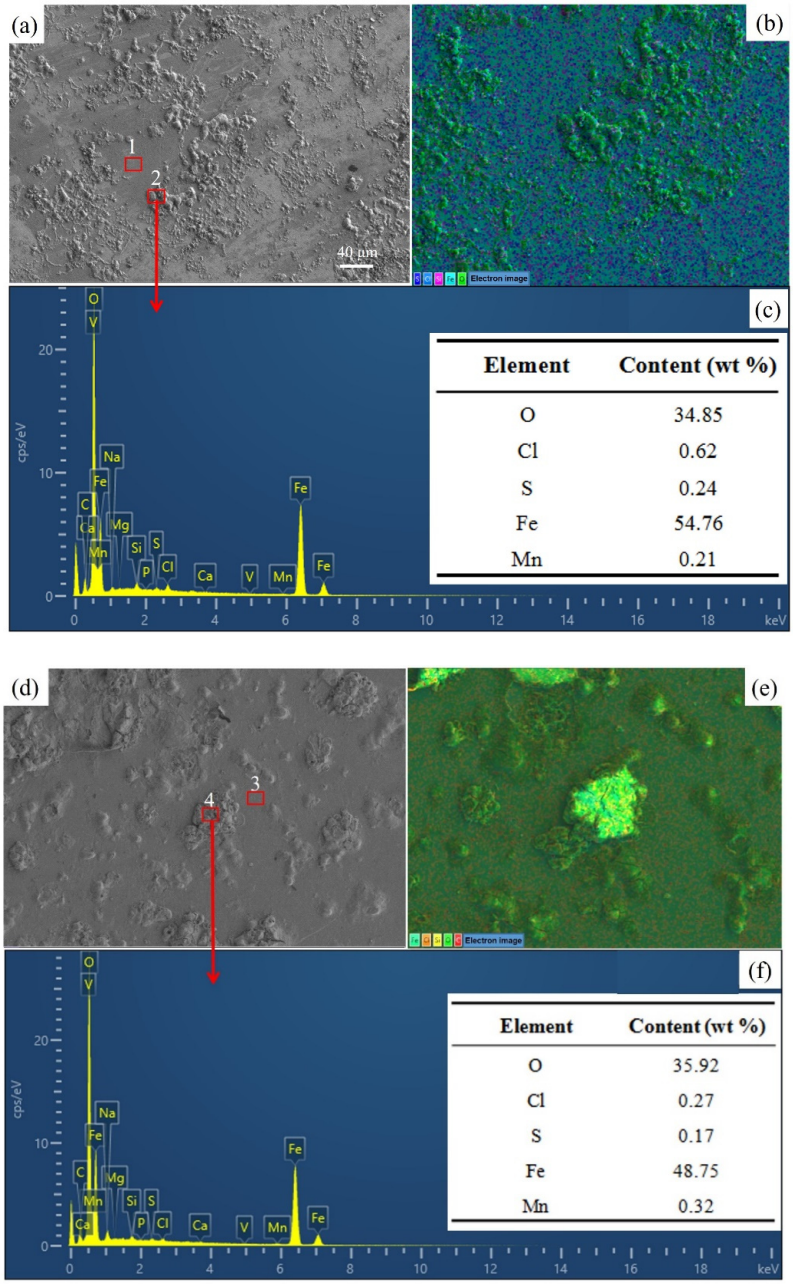

Figure 10. Locations selected for EDS analysis of (**a**) URWJB and (**d**) URWJA, local EDS spectra of (**b**) URWJB and (**e**) URWJA, and (**c**) EDS elemental mapping of (**c**) URWJB and (**f**) URWJA.

Table 6. Element content from EDS test corresponding to URWJs by FBW (wt. %).

Location No.	Sample	O	Cl	S	Fe	Mn
1	The product-free microzone of URWJB	5.06	0.19	0.04	86.37	1.10
2	Corrosion product of URWJB	34.85	0.62	0.24	54.76	0.21
3	The product-free microzone of URWJA	5.54	0.04	0.07	86.48	1.00
4	Corrosion product of URWJA	35.92	0.27	0.17	48.75	0.32

Dispersive corrosion products were distributed on the entire surface of the URWJB (Figure 10a–c) and some dense corrosion products were found at the local site of the URWJA (Figure 10d–f). It can be seen from Table 6 that the concentrations of Cl and S in the URWJB are higher than those in the URWJA, which is fully consistent with the EIS results. Noticeably, Cl and S on the surface of the welded joints were mostly distributed around the grain boundaries. The corrosion behaviour is largely governed by thermodynamics, that is, the Gibbs free energy related to oxidation and chloride and sulphide formation, ΔG_f [36]. In the URWJB samples, heterogeneous tissue and coarse grains increase the driving force ($-\Delta G_f$) of adsorption and erosion compared to the URWJA samples; thus, more Cl and S adhere to the surface. Furthermore, chloride ions (Cl^-) have strong erosive properties, and during the corrosion process, Cl^- can penetrate the passivation film and maintain corrosion through cracks and grain boundaries (as shown in Figure 11). The more loosely bound a corroded surface is, the more easily it is to be shed from the matrix, leading to further corrosion after shedding. In contrast, dense films act as protective coatings to prevent further corrosion. Therefore, we can further verify that the URWJA is more corrosion-resistant than the URWJB.

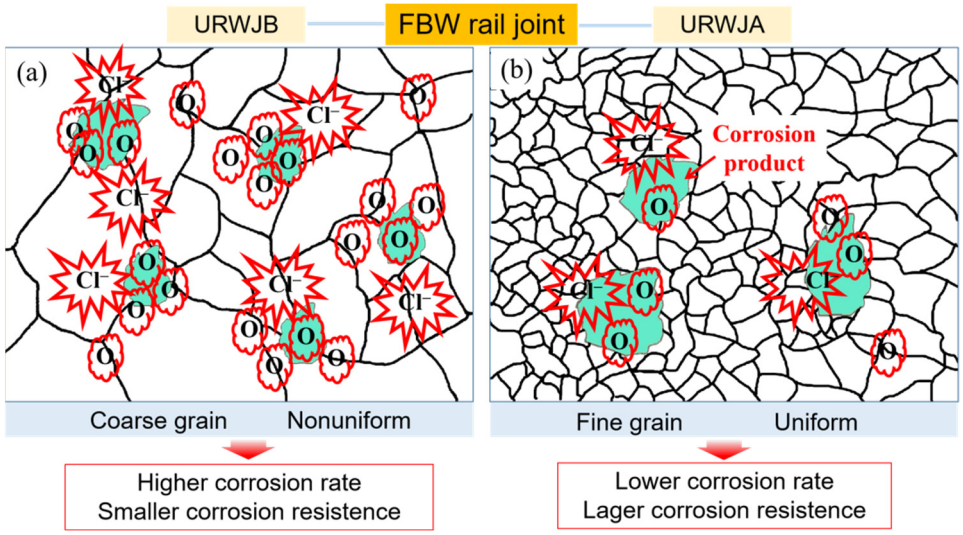

Figure 11. Schematic diagram showing the galvanic corrosion of URWJs: (**a**) URWJB, (**b**) URWJA.

4. Conclusions

In this study, the effect of the steel normalisation process on the electrochemical behaviour of the URWJs from FBW was evaluated. The major conclusions drawn from this study are as follows:

(1) After the normalising process, the URWJs had smaller and more homogeneous grains, and the average grain diameter changed from 90 μm to 16 μm;
(2) Although the maximum hardness value of the URWJB is larger than that of the URWJA, the URWJB has a more uniform hardness value distribution;
(3) Compared with BM, URWJs exhibited higher self-corrosion currents, more negative self-corrosion potentials, and lower impedance values, indicating better corrosion resistance;

(4) According to the polarisation curve, the URWJA exhibited a smaller self-corrosion current and easier passivation, indicating a lower corrosion rate and better corrosion resistance;
(5) According to the EIS results, the diameter of the capacitive loops, the maximum phase angle, and the |Z| values increased, indicating better corrosion resistance after normalisation in the marine environment;
(6) The finer grains of the normalised joints showed fewer corrosion products, denser passivation films, and less Cl^- erosive effects on the cracks and grain boundaries, thus reducing the corrosion rate of the joints.

Author Contributions: Conceptualization, Q.L. and G.G.; methodology, X.Z.; validation, X.Z. and T.L.; formal analysis, X.Z. and T.L.; investigation, X.Z. and T.L.; resources, X.Z.; data curation, X.Z. and T.L.; writing—original draft preparation, X.Z.; writing—review and editing, T.L.; supervision, Q.L. and G.G.; project administration, Q.L.; funding acquisition, G.G. All authors have read and agreed to the published version of the manuscript.

Funding: This research was jointly sponsored by the Research and Development Project of Electromagnetic Ultrasonic Welding Residual Stress Testing Equipment (2682022ZTPY003) and Fundamental Research Funds for the Central Universities—Special Research Projects (Basic Office)—Cultivation Project of Original Scientific Instruments and Equipment in 2021.

Data Availability Statement: Not applicable.

Acknowledgments: We would like to thank Hu Z.M. at Analysis and Testing center of Southwest Jiaotong University for her assistance with taking SEM images.

Conflicts of Interest: The authors declare no conflict of interest to this work. We declare that we do not have any commercial or associative interest that represents a conflict of interest in connection with the work submitted.

Abbreviations

FBW	Flash butt welding
URWJs U75V	Welded joints
URWJB U75V	Welded joints before the normalisation process
URWJA U75V	Welded joints after the normalisation process
BM	Base metal
HAZ	Heat-affected zone
WM	Weld metal
EIS	Electrochemical impedance spectroscopy

References

1. Jiang, Q.; Guojing, X.U.; Jingpo, Y.U.; Shu, F.; Zhao, H.; Materials, S.O. Study on Microstructure and Mechanical Properties of Flash Butt Welded Joint of NS700 Acid-resistant Steel. *Hot Work. Technol.* **2017**, *46*, 220–226.
2. Porcaro, R.R.; Faria, G.L.; Godefroid, L.B.; Apolonio, G.R.; Cândido, L.; Pinto, E.S. Microstructure and mechanical properties of a flash butt welded pearlitic rail. *J. Mater. Process. Technol.* **2019**, *270*, 20–27. [CrossRef]
3. Sarikavak, Y.; Turkbas, O.S.; Cogun, C. Influence of welding on microstructure and strength of rail steel. *Constr. Build. Mater.* **2020**, *243*, 118220. [CrossRef]
4. Ding, H.; Dai, J.; Dai, T.; Sun, Y.; Lu, T.; Li, M.; Jia, X.; Huang, D. Effect of preheating/post-isothermal treatment temperature on microstructures and properties of cladding on U75V rail prepared by plasma cladding method. *Surf. Coat. Technol.* **2020**, *399*, 126122. [CrossRef]
5. Zhang, B.; Wang, H.; He, B.; Ma, C.; Li, A.; Liu, D. Microstructure and mechanical properties of directed energy deposited U75V/15–5PH structurally graded material. *J. Alloy. Compd.* **2022**, *898*, 163001. [CrossRef]
6. Zhou, L.; Wang, W.J.; Hu, Y.; Marconi, S.; Rindi, A. Study on the wear and damage behaviors of hypereutectoid rail steel in low temperature environment. *Wear* **2020**, *456–457*, 203365. [CrossRef]
7. Bagheri, B.; Abbasi, M.; Abdollahzadeh, A. Microstructure and mechanical characteristics of AA6061-T6 joints produced by friction stir welding, friction stir vibration welding and tungsten inert gas welding: A comparative study. *Int. J. Miner. Metall. Mater.* **2021**, *28*, 450–461. [CrossRef]

8. Jian, H.; Wang, Y.; Yang, X.; Xiao, K. Microstructure and fatigue crack growth behavior in welding joint of Al-Mg alloy. *Eng. Fail. Anal.* **2021**, *120*, 105034. [CrossRef]
9. Liu, F.C.; Hovanski, Y.; Miles, M.P.; Sorensen, C.D.; Nelson, T.W.; Department of Mechanical Engineering Brigham. A review of friction stir welding of steels: Tool, material flow, microstructure, and properties. *J. Mater. Sci. Technol.* **2018**, *1*, 43–61. [CrossRef]
10. Yang, M.; Lu, J.; Chen, J.; Li, Y.; Yang, H. Effect of welding speed on microstructure and corrosion resistance of Al–Li alloy weld joint. *Mater. Corros.* **2019**, *71*, 300–308. [CrossRef]
11. Wang, J.; Zhang, B.; Xu, W.; Zhang, J.; Yang, L.; Peng, Z.; Hou, B. Microstructure refinement on crevice corrosion of high-speed rail steel U75V visualized by in-situ monitoring system. *Front. Mater.* **2022**, *8*, 820721. [CrossRef]
12. Xu, W.; Deng, Y.; Zhang, B.; Zhang, J.; Peng, Z.; Hou, B.; Duan, J. Crevice corrosion of U75V high-speed rail steel with varying crevice gap size by in-situ monitoring. *J. Mater. Res. Technol.* **2022**, *16*, 1856–1874. [CrossRef]
13. Zhao, X.; Fan, Y.; Liu, Y.; Wang, H.; Dong, P. Evaluation of fatigue fracture mechanism in a flash butt welding joint of a U75V type steel for railroad applications. *Eng. Fail. Anal.* **2015**, *55*, 26–38. [CrossRef]
14. Zou, D.; Yang, Q.; Lu, G. *Rail Failure Analysis and Damage Maps*; China Railway: Beijing, China, 2019; pp. 96–97. ISBN 978-7-113-11473-2.
15. Shamsudeen, S.; John, E.R.D. Effect of Welding on Pitting and Intergranular Corrosion Behavior of Marine Grade Aluminum Alloy. *Mater. Perform. Charact.* **2019**, *8*, 20180118. [CrossRef]
16. Sulaiman, S.A.; Abdullah, B.; Alias, S.K.; Ahmad, N.N.; Aziz, M.N.A. Investigation of Corrosion Rate for Different Type of Welding Joints using Shielded Metal Arc Welding (SMAW). *IOP Conf. Ser. Mater. Sci. Eng.* **2020**, *834*, 012055. [CrossRef]
17. Ding, J.; Zhang, Z.M.; Wang, J.Z.; Wang, J.Q.; Han, E.H. Corrosion behavior of different parts of the weld of 316L/52M/A508 dissimilar metal welded joint in simulated pressurized water reactor primary water. *Mater. Corros.* **2016**, *66*, 1435–1444. [CrossRef]
18. Dudzik, K.; Jurczak, W. Influence of Friction Stir Welding on Corrosion Properties of Aw-7020M Alloy in Sea Water. *Adv. Mater. Sci.* **2015**, *15*, 7–13. [CrossRef]
19. Zeng, C.Y.; Zhang, Y.P.; Hu, J.L.; Hou, B.; Wang, H.Y.; Dong, C.; Zhou, Y. The role of microstructure on corrosion fatigue behavior of thick-plate Ti–6Al–4V joint via vacuum electron beam welding. *Vacuum* **2020**, *182*, 109714. [CrossRef]
20. Mahmoud Zaghloul, M.Y.; Yousry Zaghloul, M.M.; Yousry Zaghloul, M.M. Physical analysis and statistical investigation of tensile and fatigue behaviors of glass fiber-reinforced polyester via novel fibers arrangement. *J. Compos. Mater.* **2022**. [CrossRef]
21. Sinhmar, S.; Dwivedi, D.K. A study on corrosion behavior of friction stir welded and tungsten inert gas welded AA2014 aluminium alloy. *Corros. Sci.* **2018**, *133*, 25–35. [CrossRef]
22. Xu, Y.; Hou, X.; Shi, Y.; Zhang, W.; Gu, Y.; Feng, C.; Volodymyr, K. Correlation between the microstructure and corrosion behavior of copper/316 L stainless-steel dissimilar-metal welded joints. *Corros. Sci.* **2021**, *191*, 109729. [CrossRef]
23. Liu, L.; Xu, R. Investigation of corrosion behavior of Mg-steel laser-TIG hybrid lap joints. *Corros. Sci.* **2012**, *54*, 212–218. [CrossRef]
24. Ziemian, C.W.; Sharma, M.M.; Whaley, D.E. Effects of flashing and upset sequences on microstructure, hardness, and tensile properties of welded structural steel joints. *Mater. Des.* **2012**, *33*, 175–184. [CrossRef]
25. Bauri, L.F.; Alves, L.H.D.; Pereira, H.B.; Tschiptschin, A.P.; Goldenstein, H. The role of welding parameters on the control of the microstructure and mechanical properties of rails welded using FBW. *J. Mater. Res. Technol.* **2020**, *9*, 8058–8073. [CrossRef]
26. *TB/T 1632-2014*; Railway Applications-Track-Flash Butt Welding of Rails. China Railway: Beijing, China, 2014.
27. *TB/T 2344-2020*; Rails—Part 1: 43 kg/m~75 kg/m Rails. China Railway: Beijing, China, 2020.
28. Bijanrostami, K.; Barenji, R.V. Underwater dissimilar friction stir welding of aluminum alloys: Elucidating the grain size and hardness of the joints. *Proc. Inst. Mech. Eng. Part L J. Mater. Des. Appl.* **2019**, *233*, 763–775. [CrossRef]
29. Liang, W.X.; Xian, Y.Z.; Yue, X.F.; Wei, J.S.; Peng, W.; Cheng, J.; Xiong, X.; Song, Y.; Yu, L.S. Microstructure and Mechanical Properties of Friction Stir-Welded Dissimilar Joints of ZK60 and Mg-4.6Al-1.2Sn-0.7Zn Alloys. *Materials* **2021**, *15*, 23–38.
30. Wang, Z.; Zhou, Z.Q.; Zhang, L.; Hu, J.Y.; Zhang, Z.R.; Lu, M.X. Effect of pH on the Electrochemical behavior and Passive Film Composition of 316L Stainless Steel. *Acta Metall. Sin. (Engl. Lett.)* **2019**, *32*, 585–598. [CrossRef]
31. Rovere, C.A.D.; Alano, J.H.; Silva, R.; Nascente, P.; Otubo, J.; Kuri, S.E. Characterization of passive films on shape memory stainless steels. *Corros. Sci.* **2012**, *57*, 154–161. [CrossRef]
32. Fajardo, S.; Bastidas, D.M.; Criado, M.; Bastidas, J.M. Electrochemical study on the corrosion behavior of a new low-nickel stainless steel in carbonated alkaline solution in the presence of chlorides. *Electrochim. Acta* **2014**, *129*, 160–170. [CrossRef]
33. Qiang, Y.; Zhang, S.; Guo, L.; Zheng, X.; Xiang, B.; Chen, S. Experimental and theoretical studies of four allyl imidazolium-based ionic liquids as green inhibitors for copper corrosion in sulfuric acid. *Corros. Sci.* **2017**, *119*, 68–78. [CrossRef]
34. Cui, Z.; Wang, L.; Ni, H.; Hao, W.; Man, C.; Chen, S.; Wang, X.; Liu, Z.; Li, X. Influence of temperature on the electrochemical and passivation behavior of 2507 super duplex stainless steel in simulated desulfurized flue gas condensates. *Corros. Sci.* **2017**, *118*, 31–48. [CrossRef]
35. Chen, Z.; Wei, Z.; Chen, Y.; Nong, Y.; Yi, C. Molecular insight into iron corrosion induced by chloride and sulphate. *Comput. Mater. Sci.* **2022**, *209*, 111429. [CrossRef]
36. Zahs, A.; Spiegel, M.; Grabke, H.J. Chloridation and oxidation of iron, chromium, nickel and their alloys in chloridizing and oxidizing atmospheres at 400–700 °C. *Corros. Sci.* **2000**, *42*, 1093–1122. [CrossRef]